RESEARCH ARTICLE

Wing motion measurement and aerodynamics of hovering true hoverflies

Xiao Lei Mou*, Yan Peng Liu and Mao Sun

Ministry of Education Key Laboratory of Fluid Mechanics, Beijing University of Aeronautics and Astronautics, Beijing 100191, China

*Author for correspondence (mouxiaolei@ase.buaa.edu.cn)

SUMMARY

Most hovering insects flap their wings in a horizontal plane (body having a large angle from the horizontal), called 'normal hovering'. But some of the best hoverers, e.g. true hoverflies, hover with an inclined stroke plane (body being approximately horizontal). In the present paper, wing and body kinematics of four freely hovering true hoverflies were measured using three-dimensional high-speed video. The measured wing kinematics was used in a Navier–Stokes solver to compute the aerodynamic forces of the insects. The stroke amplitude of the hoverflies was relatively small, ranging from 65 to 85 deg, compared with that of normal hovering. The angle of attack in the downstroke (~50 deg) was much larger that in the upstroke (~20 deg), unlike normal-hovering insects, whose downstroke and upstroke angles of attack are not very different. The major part of the weight-supporting force (approximately 86%) was produced in the downstroke and it was contributed by both the lift and the drag of the wing, unlike the normal-hovering case in which the weight-supporting force is approximately equally contributed by the two half-strokes and the lift principle is mainly used to produce the force. The mass-specific power was 38.59–46.3 and 27.5–35.4 W kg^{-1} in the cases of 0 and 100% elastic energy storage, respectively. Comparisons with previously published results of a normal-hovering true hoverfly and with results obtained by artificially making the insects' stroke planes horizontal show that for the true hoverflies, the power requirement for inclined stroke-plane hover is only a little (<10%) larger than that of normal hovering.

Supplementary material available online at http://jeb.biologists.org/cgi/content/full/214/17/2832/DC1

Key words: true hoverfly, hovering, wing kinematics, aerodynamics, Navier–Stokes simulation.

INTRODUCTION

Hovering is an important type of flight of insects. Most hovering insects flap their wings in a horizontal plane, called 'normal hovering' (Weis-Fogh, 1973). But some of the best hoverers (e.g. true hoverflies and dragonflies who can remain motionless at a point in the air for a long time) hover with an inclined stroke plane.

In recent years, much work has been done on aerodynamics, energetics and dynamic flight stability of insect flight and considerable progress has been achieved (e.g. Ellington et al., 1996; Liu et al., 1998; Dickinson et al., 1999; Wang, 2000; Sane and Dickinson, 2001; Sun and Tang, 2002a; Taylor and Thomas, 2003; Wang et al., 2004; Sun and Xiong, 2005; Dickson et al., 2008; Wu et al., 2009; Bergou et al., 2010; Walker et al., 2010). Most of the previous studies, however, have focused on, or are related to, normal hovering, and studies on hovering with an inclined stroke plane are very few. One reason for this is that there is a lack of wing motion data on this type of hovering.

There have been some studies on measuring the wing motion in insects hovering with an inclined stroke plane. Norberg measured the wing-tip kinematics of a freely hovering dragonfly using one high-speed camera, and obtained the stroke plane angle, stroke frequency, stroke angle and elevation angle (Norberg, 1975). Wakeling and Ellington made similar measurement for dragonflies and damselflies in near-hovering and forward flight (Wakeling and Ellington, 1997). Ellington measured the wing-tip kinematics of a true hoverfly in free hovering flight using one camera, and also obtained data on stroke plane angle, stroke frequency, stroke angle and elevation angle (Ellington, 1984b). In these works (Norberg, 1975; Wakeling and Ellington, 1997; Ellington, 1984b), because

only one camera was used, the continuous time variation of wing orientation (wing angle of attack, wing rotation rate at stroke reversal, etc.) could not be obtained. Wing angle of attack and its rate are important parameters for determining aerodynamic force, and without data on these parameters, wing motion could not be described. Recently, Wang and Russell obtained the continuous time variation of wing angle of attack, in addition to the stroke angle and elevation angle, of hovering dragonflies using three high-speed cameras (Wang and Russell, 2007). However, because of difficulty in handling the insects, only the case of tethered flight was considered.

Because, as aforementioned, some excellent hoverers hover with an inclined stroke plane, it is of great interest to obtain detailed free-flight wing kinematic data and study the aerodynamic mechanisms, power requirements and other problems related to this type of hovering. In the present study, we measured the time course of the three-dimensional (3-D) wing motion of hovering true hoverflies using three orthogonally aligned high-speed cameras and the required morphological data. On the basis of the measured data, we used computational fluid dynamics (CFD) to compute the aerodynamic forces of the flapping wings and the power required for hovering, and to compute the aerodynamic derivatives and analyse the dynamic properties of the flight system. Comparison between the computed results and the force balance condition (vertical force being equal to the weight) can provide a test of the computational model; analyzing the time courses of the wing motion, aerodynamic forces and flow fields can provide insights into the aerodynamic force production mechanism; comparing the power requirement of the inclined stroke-plane hovering with that of normal

hovering could answer the interesting question of whether power required for these two types of hovering is very different; and comparing the dynamic flight stability properties of the inclined stroke-plane hovering with that of normal hovering might provide insight into the maneuverability associated with the two types of hovering.

MATERIALS AND METHODS
Animals and 3-D high-speed filming

We netted hoverflies *Episyrphus baltealus* (De Geer, 1776) in a suburb of Beijing in June 2010. All experiments were conducted on the same day of capture. Only the most vigorous individuals were selected for the experiments.

We filmed the hovering flight of the hoverflies in an enclosed flight chamber using three orthogonally aligned synchronized high-speed cameras (MotionXtra HG-LE, Redlake MASD, Inc., San Diego, CA, USA; 5000 frames s^{-1}, shutter speed 50 μs, resolution 512×320 pixels) mounted on an optical table. The flight chamber, a cube of 15×15×15 cm^3, was built from translucent glass. We backlit each camera view using densely packed arrays of light emitting diode (LED) covered with diffusion paper. We used LED arrays as the light source because they produced much less heat than cine lights at the elevated light levels required for high-speed filming. We manually triggered the synchronized cameras when the insect was observed to hover in the approximately 5×5×5 cm^3 cubic zone at the central region of the chamber, which represented the intersecting field of views of the three cameras.

Measurement of wing and body kinematics

After the flight events were recorded, a method was required to extract the 3-D body and wing kinematics from the filmed data. The method we used here was the same as that used by Fry and others (Fry et al., 2005; Liu and Sun, 2008) [for recent development of the measuring methods, see Belhaoua et al. (Belhaoua et al., 2009), Ristroph et al. (Ristroph et al., 2009) and Walker et al. (Walker et al., 2009)]. The method is described in detail in the Appendix and is outlined here. The body and wings were represented by models (see Appendix), e.g. the model of a wing was the outline of the wing obtained by scanning the cut-off wing (Fig. 1A). We developed an interactive graphic user interface using MATLAB (v. 7.1, The Mathworks, Inc., Natick, MA, USA) to extract the 3-D body and wing positions from the frames recorded by the three cameras (an example of the frames is shown in Fig. 1B). The positions and orientations of the models of the body and wings were adjusted until the best overlap between a model image and the displayed frame was achieved in three views (the fitting process was done manually). At this point, the positions and orientations of these models would be taken as the positions and orientations of the body and the wings.

Errors in the method came from several sources. One was the deformation of the flapping wings: the wings were not flat-plate wings as they were modeled in the method (as described in the Appendix and mentioned above, the model of a wing was the outline of the wing obtained by scanning the cut-off wing, which was necessarily of a flat plate). Other error sources included errors due to camera model inaccuracy (a pinhole model was used to characterize the camera), camera calibration, stereo rig calibration, and discretization. It was shown that errors due to camera model inaccuracy, camera calibration and stereo rig calibration were small (see Appendix), and the primary errors of the method were errors due to wing deformation and discretization. We estimated the wing deformation and discretization errors as a whole by applying the
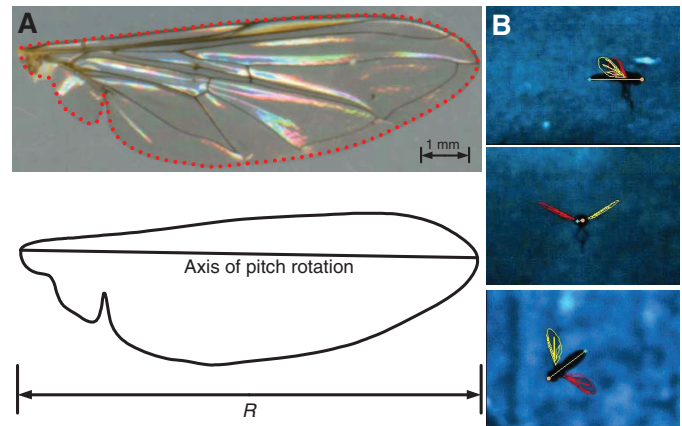

Fig. 1. (A) Wing model. *R*, wing length. (B) Example of frames recorded by the three cameras and the wing and body models.

method to a computer-generated virtual insect, which had similar wing motion as the hoverflies (see Appendix). Based on the observation of the flight of many insects (Ellington, 1984b; Ennos, 1989a; Walker et al., 2009), the wing deformation of the virtual insect was assumed to have a 15 deg twist and 6% camber during the translation phase of the downstroke or upstroke and the twist and camber increased to 25 deg and 10%, respectively, at stroke reversal. Analysis showed that errors in positional angle and elevation angle of the wing were within 3 deg and errors in pitch angle (or angle of attack) were within 4 deg (see Appendix).

Measurement of morphological parameters

The present method of measuring the morphological parameters follows, for the most part, that given by Ellington, whose paper can be consulted for a more detailed description of the method (Ellington, 1984a).

The insects were killed with ethyl acetate vapor after filming. The total mass (*m*) was measured to an accuracy of ±0.01 mg. The wings were then cut from the body and the mass of the wingless body was measured. The wing mass (m_{wg}) was determined from the difference between the total mass and the mass of wingless body.

Immediately after the wings were cut from the body, the shape of one of them was scanned using a scanner (HP scanjet 4370; resolution 3600×3600 d.p.i.). A sample of the scanned picture of a wing is shown in Fig. 1A. Using the scanned picture, wing length (*R*, the distance between the wing base and the wing tip) and local wing chord length were measured to an accuracy greater than ±0.5%. Parameters including wing area, mean chord length and radius of second moment of wing area were computed using the measured wing shape.

The wingless body was scanned from two perpendicular directions (the dorsoventral and lateral views; Fig. 2). Following Ellington (Ellington, 1984a; Ellington, 1984b), the cross-section of the body was taken as an ellipse and a uniform density was assumed for the body. With these assumptions and the measured body shape, the center of mass of body could be estimated. Body length (l_b) and distance between the wing roots (l_r) were measured from the dorsal views; distance between the wing-base axis and the center of mass (l_1) and distance between the wing-base axis and the long axis of the body (h_1) were measured from the lateral view (using these data, moments and products of inertia about the center of mass were also estimated).
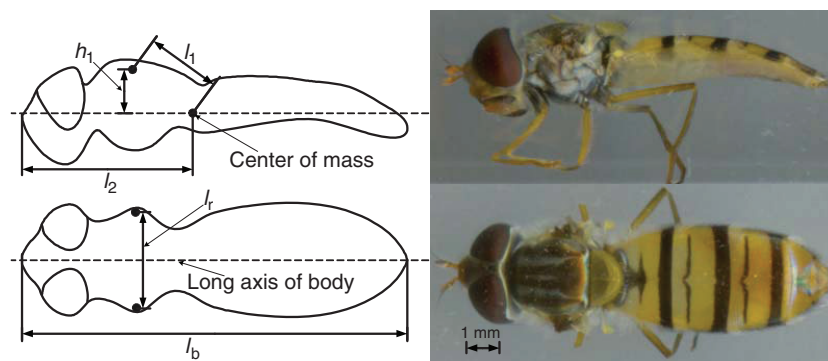
Fig. 2. Morphological parameters of the wing and body. h_1, distance from the wing-root axis to the long axis of the body; l_1, distance from the wing-root axis to the center of mass of the body; l_2, distance from anterior end of the body to the center of mass; l_b, body length; l_r, distance between two wing roots.

Computation of aerodynamic forces and power requirements

The aerodynamic forces and moments were computed using the CFD method. Under hovering flight conditions, Aono and others showed that interaction between wing and body was negligibly small: the aerodynamic force in the case with the body–wing interaction was less than 2% different from that without body–wing interaction (Aono et al., 2008; Yu and Sun, 2009). Although the left and right wings might interact *via* a 'clap and fling' mechanism, this mechanism was irrelevant in the present study because of small stroke amplitude. Therefore, in the present CFD model, the body was neglected and only the flows around one wing were computed (the aerodynamic forces produced by the other wing were derived from the results of the computed wing). Recently, Walker et al. measured the deformation of the wings of freely hovering hoverflies (Walker et al., 2010). Using Walker et al.'s data, Du and Sun investigated the effect of wing deformation on aerodynamic forces in hovering hoverflies and showed that as a first approximation, the deformable wing could be modeled by a rigid flat-plate wing with its angle of attack being equal to the local angle of attack at the radius of second moment of wing area (Du and Sun, 2010). Thus in the CFD model, we further assumed that wings were rigid flat-plate wings; the planform of the wing was obtained from the measured data, and the wing section was a flat plate with a thickness of 3% of the chord length and with rounded leading and trailing edges.

The flow equations and solution method were the same as those used in Sun and Tang (Sun and Tang, 2002a) and the method was developed by Rogers and others (Rogers and Kwak, 1990; Rogers et al., 1991). In the method, the time derivatives of the momentum equations ware differenced using a second-order, three-point backward difference formula. To solve the time-discretized momentum equations for a divergence free velocity at a new time level, a pseudo-time level was introduced into the equations and a pseudo-time derivative of pressure divided by an artificial compressibility constant was introduced into the continuity equation. The resulting system of equations was iterated in pseudo-time until the pseudo-time derivative of pressure approached zero and, thus, the divergence of the velocity at the new time level approached zero. The derivatives of the viscous fluxes in the momentum equation were approximated using second-order central differences. For the derivatives of convective fluxes, upwind differencing based on the flux-difference splitting technique was used. A third-order upwind differencing was used at the interior points and a second-order upwind differencing was used at points next to boundaries. Details of this algorithm can be found in previous studies (Rogers and Kwak, 1990; Rogers et al., 1991).

The computational grids (OH type) were generated using a Poisson solver, which was based on the work of Hilgenstock

(Hilgenstock, 1988). The grids will be further described in the Results and discussion section as will analysis of the convergence of solutions.

Boundary conditions were as follows. For the far-field boundary condition, at inflow boundary, the velocity components were specified as free-stream conditions (determined by flight speed), whereas pressure was extrapolated from the interior; at the outflow boundary, pressure was set equal to the free-stream static pressure and velocity was extrapolated from the interior. On the wing surface, impermeable wall and non-slip conditions were applied and the pressure was obtained through the normal component of the momentum equation written in the moving grid system.

Solving the Navier–Stokes equations yielded the fluid velocity and pressure at discretized grid points and time steps. The aerodynamic forces acting on the wing were calculated from the pressure and the viscous stress on the wing surface.

RESULTS AND DISCUSSION

Four hoverflies hovering at the central region of the flight chamber (the zone of the intersecting field of view of the three cameras) were filmed. They were denoted as HF1, HF2, HF3 and HF4, respectively. All of the hoverflies except HF2 were female. For each of the hoverflies, film of approximately six wing strokes were digitized.
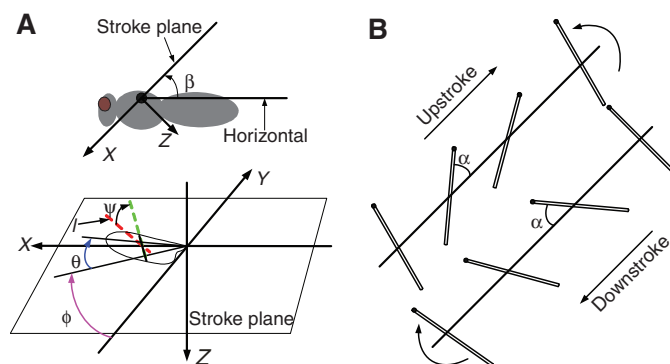

Fig. 3. (A) Angles of a flapping wing that determine the wing orientation. The (X, Y, Z) coordinates are in a system with its origin at the wing root; the Y-axis points to the side of the insect and the X–Y plane coincides with the stroke plane. l, a line that is perpendicular to the wing span and parallel to the stroke plane; β, stroke plane angle; φ, ψ and θ: positional angle, pitch angle and deviation angle of the wing, respectively. (B) A wing stroke diagram highlighting the motion of the wing chord during a typical stroke (the black circle represents the leading edge). α, angle of attack of the wing (α=ψ in the downstroke, α=180−ψ in the upstroke).

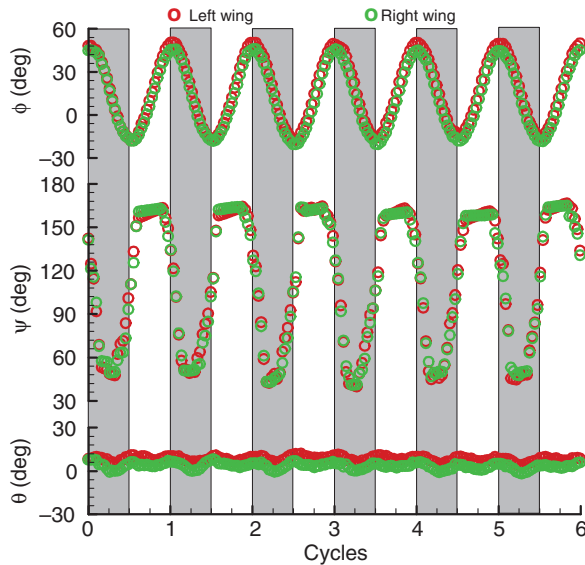Fig. 4. Instantaneous wing kinematics of hoverfly HF1 in hovering. ϕ, positional angle; ψ, pitch angle; θ, deviation angle.

Samples of the original video sequences for HF1 are presented as supplementary material Movie 1.

Wing kinematics

We determined the stroke plane in the same way as Ellington (Ellington, 1984b). In a wingbeat cycle, approximately 35 pictures were taken and the same number of points on the curve traced by the wing tip was determined. We projected all the wing-tip points of both the left and right wings in the six wingbeats onto the plane of symmetry of the insect. A linear regression line of these projected points on the plane of symmetry was then determined. The stroke plane was defined as a plane that passed the two wing roots and was parallel to the above line. This plane is tilted at an angle β to the horizontal (called the stroke plane angle). The angles determining the wing orientation are defined as follows. A line is drawn between the wing base and wing tip (see Fig. 1A and Fig. 3A). Let (X, Y, Z) be a reference frame with origin at the wing base and an $X–Y$ plane coinciding with the stroke plane (Fig. 3). The orientation of the wing is determined by the three Euler angles: positional angle (ϕ), stroke deviation angle (θ) and pitch angle (ψ) (see Fig. 3A), where ϕ is the angle between the projection of the line joining the wing base and wing tip onto the stroke plane and the Y-axis, θ is the angle between the line joining the wing base and wing tip and its projection onto the stroke plane, and ψ is the angle between the local wing chord and line l (l is perpendicular to the wing span and parallel to the stroke plane). ψ is related to the angle of attack of the wing (α) as follows: in the downstroke, $\alpha=\psi$; in the upstroke, $\alpha=180-\psi$. The measured data of these angles as functions of time for the left and the right wings of HF1 are shown in Fig. 4 (for each of the four insects, approximately six well-repeated wing strokes in which the left and right wings were moving symmetrically were captured). For a clear description of the data, we express time during a cycle as a non-dimensional parameter, $\hat{t}$, such that $\hat{t}=0$ at the start of a downstroke and $\hat{t}=1$ at the end of the subsequent upstroke. Fig. 5 plots the phase-average value (mean ± s.d.) of the positional angle (averaged over six wingbeat cycles) for each hoverfly against non-dimensional time. Figs 6 and 7 give the corresponding data for the pitch angle and the deviation angle, respectively.
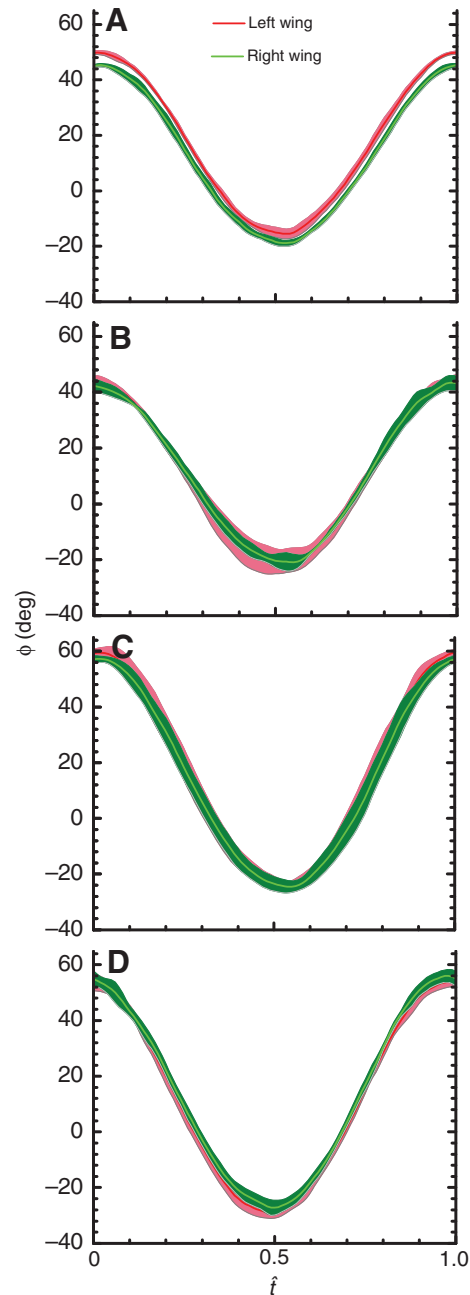

Fig. 5. Positional angle (ϕ) against non-dimensional time ($\hat{t}$) for the four hoverflies. (A) HF1; (B) HF2; (C) HF3; (D) HF4. The shaded region around each line represents the s.d. over the six wingbeats.

As seen in Figs 4–7, the motion of the right wing is approximately the same as that of the left wing, as expected for hovering flight. For a given hoverfly, the positional angle shows less variation between successive wingbeats than the geometrical angle of attack and the deviation angle.

The stroke positional angle varied with time approximately as a sinusoidal function (Fig. 5). From the data, the stroke amplitude (Φ) and mean stroke angle ($\bar{\phi}$) can be determined using the following equations: $\bar{\phi}=(\phi_{max}+\phi_{min})/2$ and $\Phi=\phi_{max}-\phi_{min}$, where ϕ_{max} and ϕ_{min} are the maximum and minimum values of ϕ, respectively (see Ellington 1984b) (Table 1). The stroke amplitude of the hoverflies ranged from 65 to 85 deg. Ellington obtained Φ for two freely
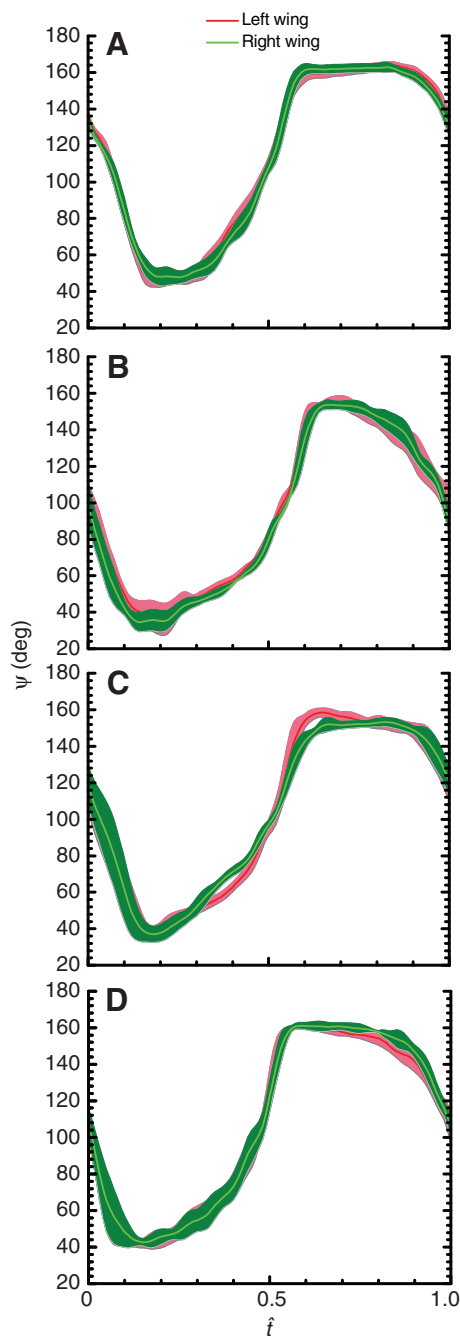
Fig. 6. Pitch angle (ψ) against non-dimensional time ($\hat{t}$) for the four hoverflies. (A) HF1; (B) HF2; (C) HF3; (D) HF4. The shaded region around each line represents the s.d. over the six wingbeats.

Fig. 7. Deviation angle (θ) against non-dimensional time ($\hat{t}$) for the four hoverflies. (A) HF1; (B) HF2; (C) HF3; (D) HF4. The shaded region around each line represents the s.d. over the six wingbeats.

hovering true hoverflies [the same species (*E. baltealus*) as in the present study]: one was in inclined hovering with Φ=66 deg and the other in normal hovering with Φ=95 deg (Ellington, 1984b). Recently, Walker and others obtained Φ for hoverflies of another species, *Eristalis tenax*, which only performed normal hovering (Walker et al., 2010; Liu and Sun, 2008); Φ ranged from approximately 70 to 115 deg (there were five individuals in Walker et al.'s experiment and three in Liu and Sun's experiment). We thus see that the stroke amplitude of hovering flies in inclined hovering is relatively small compared with that in normal hovering.
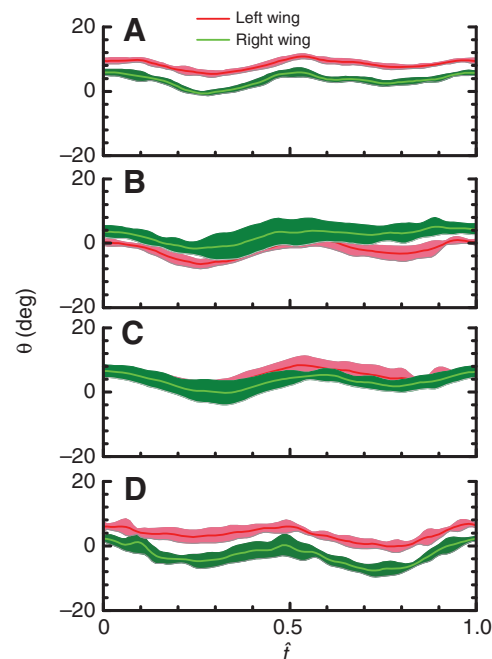
The pitch angle (Fig. 6) had very sharp variation at the stroke reversal ($\hat{t}$=0.4–0.6, 0.9–1 and 0–0.1), but varied relatively slowly in the mid-position of the downstroke or upstroke ($\hat{t}$=0.1–0.4 or 0.6–0.9). The angle of attack in the mid-position of the downstroke was approximately 50 deg, and that in the mid-position of the upstroke was approximately 20 deg. This is unlike hoverflies in normal hovering (Ellington, 1984b; Walker et al., 2010; Liu and Sun, 2008) and other normal-hovering insects (e.g. Ellington, 1984b), whose downstroke and upstroke angles of attack are not very different.

The stroke deviation angle (Fig. 7) was relatively small; it was higher at the beginning and the end of a downstroke or upstroke, and lower at the middle of the downstroke or upstroke, which led to a shallow U-shaped wing-tip trajectory (the mean deviation angle was approximately 6, 0, 4 and 1 deg for HF1, HF2, HF3 and HF4, respectively, and the amplitude of the deviation angle was approximately 4, 5, 5 and 6 deg for the four insects, respectively).

The wingbeat frequency (*f*), stroke plane angle (β) and body angle (χ) are also given in Table 1 [the body angle is the angle between the long axis of the body and the horizontal, see Ellington (Ellington, 1984b)].

The insects filmed in the present study were only in approximate hovering, i.e. some of them moved at very low velocity. The non-dimensional velocity of the body motion, denoted by advance ratio (*J*), was measured as the velocity of the body motion divided by the mean wing-tip speed 2Φ*fR*; the values of *J* are also included in Table 1. *J* was very small for HF1, HF3 and HF4, not more than 0.07. For HF2, *J* was 0.13 and the insect was in slow forward flight. However, its wing kinematics was not very different from that of the other insects, except for the upstroke pitch angle: for HF1, HF3 and HF4, ψ was approximately constant in the mid-upstroke ($\hat{t}$≈0.6–0.9) and the wing started to pitch at $\hat{t}$≈0.9, whereas for HF2, the wing started to pitch much earlier, at $\hat{t}$≈0.7 (Fig. 6).

Table 1. Wing and body kinematic parameters (mean ± s.d.) of the hoverflies

ID	f (Hz)	Φ (deg)		$\bar{\phi}$ (deg)		β (deg)	χ (deg)	J
		Left	Right	Left	Right			
HF1	162±2	65.9±1.3	65.2±1.3	17.2±1.7	13.5±1.2	34.4	−0.9±0	0
HF2	183±2	66.2±2.9	63.9±2.1	11.5±1.6	10.7±0.4	29.0	14.0±0.5	0.13
HF3	186±2	86.1±3.7	84.0±3.6	18.0±1.1	16.7±1.1	21.6	8.5±1.0	0.07
HF4	164±3	84.2±2.2	83.4±2.1	12.6±1.2	14.4±1.1	25.3	11.6±0.4	0.06

HF1, HF2, HF3 and HF4, hoverflies 1, 2, 3 and 4, respectively (HF2, male; others, female); J, advance ratio; f, stroke frequency; β, stroke plane angle; χ, body angle; Φ, stroke amplitude; $\bar{\phi}$, mean stroke angle.

Table 2. Morphological parameters of the hoverflies

ID	m (mg)	m_{wg} (mg)	R (mm)	S (mm^2)	l_b (mm)	h_1/l_b	l_1/l_b	l_2/l_b	l_r/l_b	r_2/R	$I_{x,b}$ (kg m^2)	$I_{y,b}$ (kg m^2)	$I_{z,b}$ (kg m^2)	$I_{xz,b}$ (kg m^2)
HF1	22.08	0.285	9.70	21.88	11.04	0.06	0.15	0.42	0.26	0.574	1.48×10^{-11}	1.79×10^{-10}	1.83×10^{-10}	5.85×10^{-12}
HF2	23.63	0.225	9.68	19.96	10.64	0.05	0.11	0.41	0.28	0.576	1.51×10^{-11}	1.73×10^{-10}	1.75×10^{-10}	2.40×10^{-12}
HF3	10.39	0.105	6.93	11.87	8.13	0.06	0.13	0.41	0.26	0.567	3.97×10^{-12}	4.70×10^{-11}	4.77×10^{-11}	1.21×10^{-12}
HF4	10.41	0.195	7.13	12.17	8.75	0.04	0.10	0.39	0.26	0.577	4.25×10^{-12}	5.07×10^{-11}	5.13×10^{-11}	1.92×10^{-12}

HF1, HF2, HF3 and HF4, hoverflies 1, 2, 3 and 4, respectively (HF2, male; others, female); m, mass of the insect; m_{wg}, mass of one wing; R, wing length; S, area of one wing; l_b, body length; h_1, distance from wing-root axis to long axis of body; l_1, distance from wing-root axis to body center of mass; l_2, distance from anterior end of body to center of mass; l_r, distance between two wing roots; r_2, radius of second moment of wing area; $I_{x,b}$, $I_{y,b}$, $I_{z,b}$ and $I_{xz,b}$, moments and product of inertia of the body about the center of mass.

Morphological parameters

Morphological parameters of the insects are given in Table 2. Parameters in the table include total mass (m), wing mass (m_{wg}), wing length (R), wing area (S), radius of the second moment of wing area (r_2), body length (l_b), distance between the two wing roots (l_r), distance between the wing-base axis and the center of mass (l_1), distance from the anterior end of the body to the center of mass (l_2), distance between the wing-base axis and the long axis of the body (h_1), and the moments and product of inertia of the body about its center of mass, $I_{x,b}$, $I_{y,b}$, $I_{z,b}$ and $I_{xz,b}$ (here x is an axis along the long axis of the body, pointing forward, y is an axis pointing to the right side of the body, and z is the other axis; the origin is at the center of mass of the body).

Computed aerodynamic forces

With the measured wing kinematics and using the CFD method described above, aerodynamic forces produced by the flapping wings were computed. We used a sinusoidal function to fit the data and obtain the time course of ϕ, and the first two terms and first four terms of the Fourier series to fit the data of θ and α, respectively. Let V and H be the computed vertical and horizontal forces of a wing, respectively; let L and D be the lift and drag of a wing, respectively (wing lift is the force component perpendicular to the stroke plane and wing drag is the force component in the stroke plane and perpendicular to the wing span). The force coefficients are defined as $C_V = V/0.5\rho U^2 S$, etc., where U is the mean velocity of wing at r_2 ($U = 2\Phi f r_2$) and ρ is the fluid density. The Reynolds number (Re) is 320, 330, 260 and 240 for HF1, HF2, HF3 and HF4, respectively (Re is defined as $Re = cU/\nu$, where c is mean chord length and ν is the kinematic viscosity of the air).

Before proceeding to study the flows and aerodynamic forces, we conducted a grid resolution test. Three grids were considered: $26\times25\times32$ (in the normal direction of the wing surface, around the wing section and in the spanwise direction of the wing, respectively; first layer grid thickness was $0.004c$), $52\times51\times65$ (first layer grid thickness was $0.002c$) and $100\times99\times130$ (first layer grid thickness was $0.001c$). Note that in each refinement, the grid dimension in each direction was approximately doubled. In the normal direction, the outer boundary was set at 20 chord lengths from the wing, and

in the spanwise direction, the boundary was set at six chord lengths from the wing. Portions of the dense grid ($100\times99\times130$) are shown in Fig. 8. [Note that the wing tip is slightly different from that of the real wing shown in Fig. 1, the pointed tip being cut off; without the tip cut off, the wing tip would be much narrower than the middle portion of the wing and the grid near the wing tip would have very large distortion, which would make the computation less accurate; experimental (Usherwood and Ellington, 2002) and computational (Luo and Sun, 2005) studies have shown that a slight change in wing shape had little effect on the aerodynamic force coefficients.] The non-dimensional time step was 0.02 (non-dimensionalized by c/U; the effect of time step value was studied and it was found that a numerical solution effectively independent of the time step was achieved if the time step value was ≤0.02). Calculations were
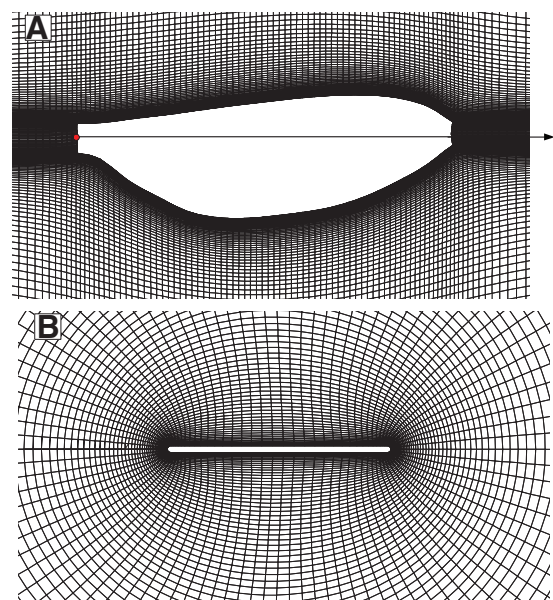

Fig. 8. Portions of the computation grid of the hoverfly wing (A) in the plane of wing planform and (B) in a sectional plane. The red circle in A indicates the wing base.
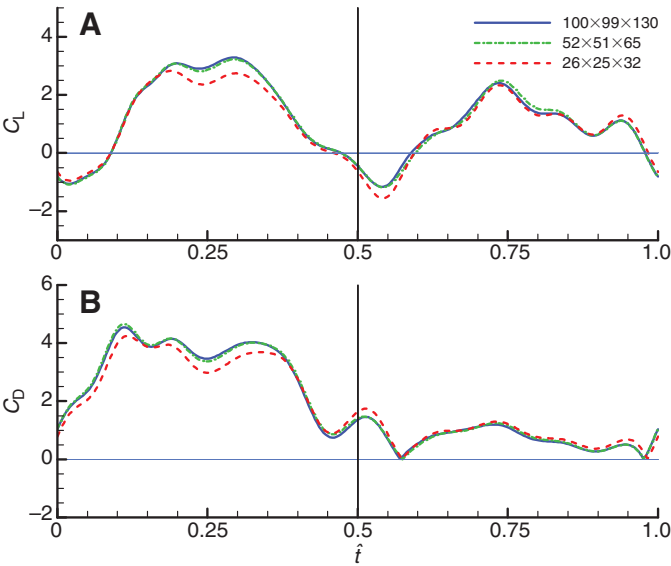
Fig. 9 Time courses of the lift (C_L) and drag (C_D) coefficients of the wing of HF1 at hovering flight for different grids. $\hat{t}$, non-dimensional time.

performed using the above grids for the hovering flight of HF1; the results are shown in Fig. 9. The first grid refinement (from grid $26\times25\times32$ to grid $52\times51\times65$) produced relatively large mean magnitudes of change in C_L and C_D of 0.19 and 0.18, respectively, but the second grid refinement (from grid $52\times51\times65$ to grid $100\times99\times130$) produced only a small change in the results (0.05 for both C_L and C_D). The ratio between the changes in C_L (0.05/0.19) and the changes in C_D (0.05/0.18) are approximately 1/4, as expected for the second-order method. Let us use the above data to give an estimate of the accuracy of the solution obtained by the largest grid ($100\times99\times130$). Suppose that the grid is further refined (doubling the grid dimension in each direction), one could expect that the changes in C_L and C_D would be approximately 0.0125 (0.05/4=0.0125). Based on the 1/4-convergence ratio, we could estimate that the solution by grid $100\times99\times130$ has errors in C_L and C_D of 0.017 [$0.0125\times(4/3)=0.017$]. The mean C_L and C_D values are 1.1 and 1.9, respectively. Therefore, it is estimated that, when using the $100\times99\times130$ grid, the numerical discretization and convergence errors in the mean C_L and C_D are approximately 1%. The $100\times99\times130$ grid was used for the present flow computations.

First, we looked at the computed mean forces and determined whether the vertical force could support the insect weight and the horizontal force was zero (time courses of the forces and flows will be examined in the next section). The computed mean vertical force and horizontal force coefficients ($\overline{C}_V$ and $\overline{C}_H$, respectively; averaged over one wingbeat cycle) are given in Table 3. The non-dimensional weight of an insect, denoted as C_G [$C_G=mg/0.5\rho U^2(2S)$] is also given

Table 3. Computed mean vertical and horizontal forces of the wings

ID	$\overline{C}_V$	$\overline{C}_H$	C_G
HF1	1.63	0.38	1.86
HF2	1.85	−0.11	1.74
HF3	1.70	0.29	1.49
HF4	1.71	0.35	1.75

HF1, HF2, HF3 and HF4, hoverflies 1, 2, 3 and 4, respectively (HF2, male; others, female); $\overline{C}_V$ and $\overline{C}_H$, mean vertical force and horizontal force coefficients, repsectively; C_G, non-dimensional weight of the insect.
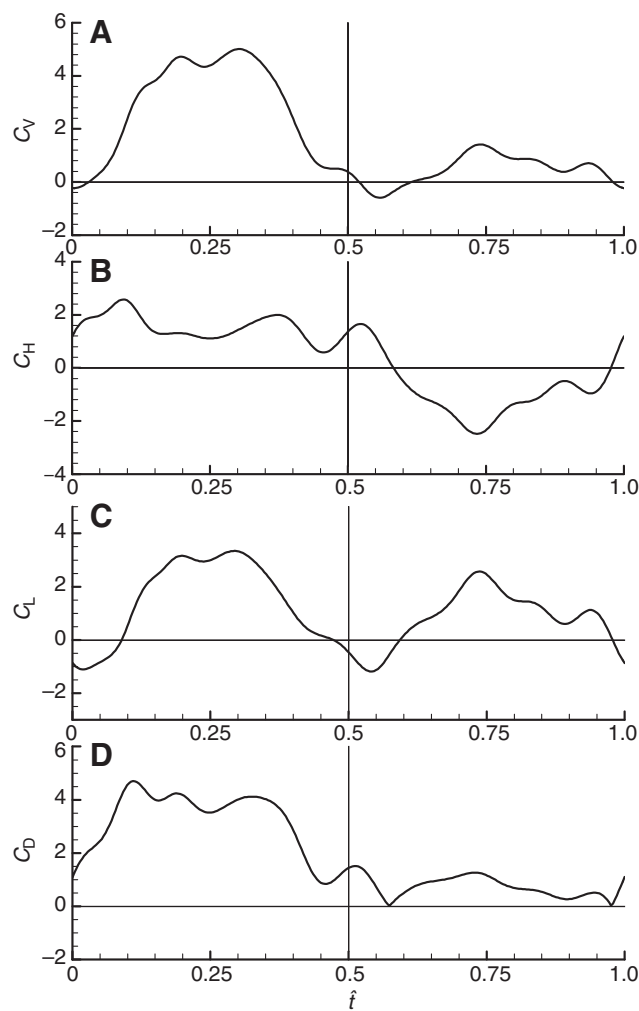

Fig. 10. Time courses of the computed force coefficients of HF1 in one cycle. C_V and C_H, vertical and horizontal force coefficients, respectively; C_L and C_D, wing lift and drag coefficients, respectively; $\hat{t}$, non-dimensional time.

in Table 3. For all four hoverflies considered, the weight balance condition was approximately met: $\overline{C}_V$ was different from C_G by less than 15% (the computed mean vertical forces of HF1 and HF4 were 12 and 2% less than the weight, respectively; those of HF2 and HF3 were 6 and 14% greater than the weight, respectively). The horizontal force balance condition was also approximately met, although a little more poorly than the case of weight balance condition (the horizontal forces of HF1, HF2, HF3 and HF4 were 20, 6, 19 and 20% of their respective weights). Possible reasons for the discrepancies include idealization in the CFD model and the fact that the insects might not be in exactly balanced flight.

Time courses of the aerodynamic forces and flows

Here we look at the time courses of the aerodynamic forces and flows and examine the properties of the aerodynamic forces. Because the wing motions of the four insects were similar, only the results for one insect, HF1, are discussed in detail here. Fig. 10 shows the time courses of C_V, C_H, C_L and C_D for HF1 in one cycle.

From Fig. 10A, it is apparent that most of the vertical force, or the weight-supporting force, is produced in the downstroke (unlike in the case of normal hovering, in which the downstroke and
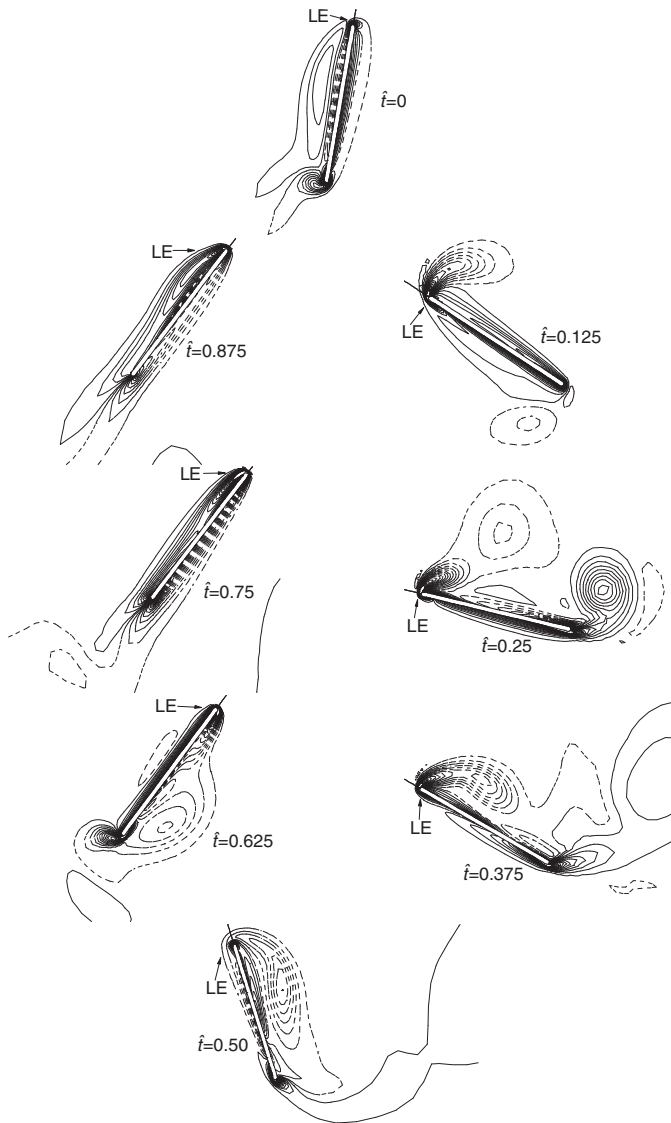
Fig. 11. Vorticity plots at spanwise location r_2 at various times during one cycle for the left wing of hoverfly HF1. Solid and broken lines indicate positive and negative vorticity, respectively. The magnitude of the non-dimensional vorticity at the outer contour is 1 and the contour interval is 3. LE, leading edge; $\hat{t}$, non-dimensional time; $\hat{t}=0$, start of downstroke (end of upstroke); $\hat{t}=0.25$, mid downstroke; $\hat{t}=0.5$, end of downstroke (start of upstroke); $\hat{t}=0.75$, mid upstroke.

downstroke (for hoverflies HF2, HF3 and HF4, this value is 89, 81 and 89%, respectively). The horizontal force produced in the downstroke is approximately the same as that in the upstroke, but they have opposite signs (Fig. 10B).

The vertical and horizontal forces of a wing are the results of the lift and drag of the wing. For HF1, the downstroke C_D is a little larger than C_L (Fig. 10C,D) (for hoverflies HF2, HF3 and HF4, C_L and C_D in the downstroke are about the same). Because the stroke plane is inclined, this means that the vertical force, or the weight-supporting force, produced in the downstroke is contributed by both the lift and the drag of the wing, unlike in the case of normal hovering, in which the weight-supporting force is mainly contributed by the lift of the wing. From data in Fig. 10C,D, it is calculated that approximately 51% of the vertical force is contributed by the drag (for hoverflies HF2, HF3 and HF4, this value is 36, 33 and 38%, respectively).

The corresponding flowfield is shown in Fig. 11. The leading-edge vortex does not shed in an entire downstroke ($\hat{t}=0$–0.5), showing that the large C_L and C_D, and hence the large vertical force (C_V) in the downstroke, are mainly due to the delayed stall mechanism.

Flight power

With the flows computed by the CFD method, the mechanical power of a wing (P) can be easily calculated:

$$P = (\mathbf{M}_a + \mathbf{M}_i)\,\mathbf{\Omega}\,. \tag{1}$$

Here, $\mathbf{M}_a$ is the aerodynamic moment about the wing root, $\mathbf{M}_i$ is the inertial moment and $\mathbf{\Omega}$ is the angular velocity vector of the wing. $\mathbf{M}_a$ is readily calculated using the force distribution obtained from the flow computation and $\mathbf{\Omega}$ is known from the measured data. The way to determine $\mathbf{M}_i$ has been described in our previous works (e.g. Sun and Tang, 2002b). In calculating $\mathbf{M}_i$, moments and products of inertia of the wing mass are needed. They are estimated using the wing mass measured in the present study and the density distribution of a dronefly wing measured previously (Ennos, 1989b); the results are given in Table 4. With the moments and products of inertia known and wing acceleration computed from $\mathbf{\Omega}$, $\mathbf{M}_i$ can be calculated.

The instantaneous non-dimensional power (C_p) and the non-dimensional aerodynamic ($C_{p,a}$) and inertial ($C_{p,i}$) power of a wing (non-dimensionalized by $0.5\rho U^2 Sc$) for HF1 are given in Fig. 12 (those for HF2, HF3 and HF4 are similar). It is interesting to note that the time course of C_p is more similar to that of $C_{p,i}$ than to that of $C_{p,a}$, because the inertial power is larger than the aerodynamic power in many parts of the stroke cycle. This means that elastic energy storage could be important for the hoverflies.

Integrating P over the part of a wingbeat cycle where it is positive gives the positive work (W^+); integrating P over the part of a wingbeat cycle where it is negative gives the negative work (W^-). The mass-specific power (P^*) is determined as the mean mechanical power over a wingbeat cycle divided by the mass of the insect. In

upstroke contribute to the weight-supporting force approximately equally); this is expected for a flapping wing with highly inclined stroke plane. From the data in Fig. 10A, it is calculated that approximately 86% of the vertical force is produced in the

Table 4. Estimated moments and products of inertia of wing mass

ID	$I_{x,w}$ (kg m^2)	$I_{y,w}$ (kg m^2)	$I_{z,w}$ (kg m^2)	$I_{xz,w}$ (kg m^2)
HF1	1.97×10^{-13}	4.96×10^{-12}	4.76×10^{-12}	2.08×10^{-13}
HF2	1.55×10^{-13}	3.89×10^{-12}	3.74×10^{-12}	1.63×10^{-13}
HF3	3.70×10^{-14}	9.32×10^{-13}	8.95×10^{-13}	3.91×10^{-14}
HF4	7.17×10^{-14}	1.81×10^{-12}	1.73×10^{-12}	7.58×10^{-14}

HF1, HF2, HF3 and HF4, hoverflies 1, 2, 3 and 4, respectively (HF2, male; others, female); $I_{x,w}$, $I_{y,w}$, $I_{z,w}$ moments of inertia of a wing about the x, y and z axes, respectively; $I_{xz,w}$, product of inertia of the wing (here x is an axis along the long axis of the wing, pointing from wing root to wing tip, y is an axis perpendicular to the wing surface, and z is an axis pointing from leading edge to trailing edge of the wing; the origin is at the wing root).
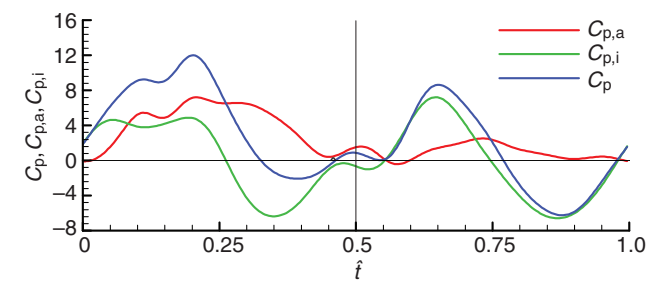
Fig. 12. Time courses of power. C_p, non-dimensional power; $C_{p,a}$ and $C_{p,i}$, non-dimensional aerodynamic and inertial power, respectively. $\hat{t}$, non-dimensional time.
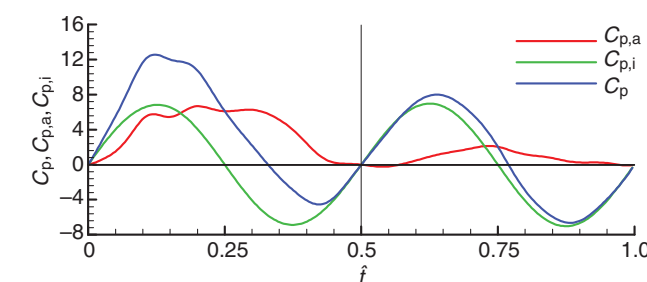

Fig. 13. Time courses of power. C_p, non-dimensional power; $C_{p,a}$ and $C_{p,i}$, non-dimensional aerodynamic and inertial power, respectively. $\hat{t}$, non-dimensional time.

the case of zero elastic energy storage, with the added assumption that the cost for dissipating the negative work is negligible, $P^*=P_1^*=W^+/t_w m$, where t_w is the wingbeat cycle. In the case of 100% elastic energy storage, $P^*=P_2^*=(W^+-|W^-|)/t_w m$.

The computed mass-specific power is given in Table 5. In the case of zero elastic energy storage, P_1^* is 39–46 W kg^{-1} for the four hoverflies; in the case of 100% elastic energy storage, P_2^* is 27–35 W kg^{-1}. For HF1, the largest possible effect of elastic energy storage reduces the power by approximately 29% (for HF2, HF3 and HF4, the values are 24, 24 and 37%, respectively).

As most of the wing mass is located near the axis of spanwise rotation of the wing and the pressure center is not far from the axis of spanwise rotation, it is expected that contribution by the spanwise rotation of the wing to the aerodynamic and inertial moments, and hence to the mechanical power, is small. Because the elevation angle is much smaller than the stroke angle, it is expected that contribution by the elevation of the wing to the mechanical power is also small. C_p, $C_{p,a}$ and $C_{p,i}$, computed by neglecting contributions by the spanwise rotation and the elevation of the wing, are shown in Fig. 13, and values of the corresponding mass-specific power are included in Table 5 (numbers in parentheses). The contributions by the spanwise rotation and the elevation of the wing are indeed small: the mass-specific power without the contributions from spanwise rotation and elevation is only approximately 5% different from that with the contributions.

True hoverflies also perform normal hovering. It is of interest to know whether there is any significant difference in power between these two types of hovering for true hoverflies. We examined this problem in two ways. First, we compared the mass-specific power of the inclined-stroke hoverflies of the present study with that from previously published normal hovering simulation studies. Sun and Du, using Ellington's wing kinematics data (Ellington, 1984b), computed the mass-specific power of a true hoverfly in normal hovering; P_1^* and P_2^* were 39 and 27 W kg^{-1}, respectively (Sun

and Du, 2003). These values are the same as those of HF1 in the present study, and a little smaller than those of HF2, HF3 and HF4. Next, we artificially changed the insects' body angle so that the stroke plane became horizontal and adjusted the downstroke and upstroke angles of attack so that the same weight-supporting force and horizontal force were produced. The corresponding power becomes 35.2–43.4 W kg^{-1} for the case of zero elastic energy storage and 25.2–34.3 W kg^{-1} for the case of 100% elastic energy storage (Table 6); these values are less than 10% smaller than those found for inclined stroke-plane hovering.

From the above comparisons, we see that for the true hoverflies, the power requirement for inclined stroke-plane hovering is only slightly (approximately 10%) larger than that of normal hovering.

Aerodynamic derivatives and flight stability analysis

With the present CFD model, aerodynamic derivatives of a hovering insect can be readily computed. With the aerodynamic derivatives and the measured morphological parameters (mass, moment of inertia, etc.; Table 2), the system matrix of the insect can be determined. The eigenvalues and eigenvectors of the system matrix give the stability properties of the flight, from which insight into flight maneuverability can be obtained. Here, we conduct a longitudinal stability analysis of the hovering flight of HF1 (among the four insects considered in the paper, HF1 has the largest inclined stroke-plane angle). A description of the stability analysis method can be found in previous studies (Taylor and Thomas, 2003; Sun and Xiong, 2005).

The longitudinal system matrix of a hovering insect (**A**) is as follows:

$$\mathbf{A} = \begin{bmatrix} X_u / m & X_w / m & X_q / m & -g \\ Z_u / m & Z_w / m & Z_q / m & 0 \\ M_u / I_{y,b} & M_w / I_{y,b} & M_q / I_{y,b} & 0 \\ 0 & 0 & 1 & 0 \end{bmatrix}, \quad (2)$$

Table 5. The computed mass-specific power

ID	P_1^* (W kg^{-1})	P_2^* (W kg^{-1})
HF1	38.52 (41.27)	27.46 (25.49)
HF2	44.20 (44.98)	33.69 (31.34)
HF3	46.30 (47.66)	35.41 (33.92)
HF4	44.10 (48.02)	27.89 (26.74)

HF1, HF2, HF3 and HF4, hoverflies 1, 2, 3 and 4, respectively (HF2, male; others, female); P_1^* and P_2^*, mass-specific power in the cases of 0 and 100% elastic energy storage, respectively. Number in the parentheses represents the mass-specific power computed by neglecting contributions due to the spanwise rotation and elevation of the wing.

Table 6. Mass-specific power when artificially changing the insects' body angle so that the stroke plane becomes horizontal

ID	P_1^* (W kg^{-1})	P_2^* (W kg^{-1})
HF1	35.15	25.18
HF2	42.18	34.34
HF3	40.64	31.85
HF4	43.37	26.69

HF1, HF2, HF3 and HF4, hoverflies 1, 2, 3 and 4, respectively (HF2, male; others, female); P_1^* and P_2^*, mass-specific power in the cases of 0 and 100% elastic energy storage, respectively.

Table 7. Non-dimensional stability derivatives

ID	X_u^+	Z_u^+	M_u^+	X_w^+	Z_w^+	M_w^+	X_q^+	Z_q^+	M_q^+
HF1	−1.71	0.22	1.96	0.22	−1.84	0.47	−0.26	−0.15	−0.15
HF1$_{rot}$	−1.31	−0.35	1.99	0.05	−1.78	−0.57	−0.31	−0.05	−0.15
HF$_{norm}$	−1.28	−0.04	2.32	0.01	−1.26	0.05	−0.28	−0.00	−0.03

HF1, hoverfly 1; HF1$_{rot}$, hoverfly 1 rotated to normal hovering; HF$_{norm}$, hoverfly studied by Sun and Wang in normal hovering (Sun and Wang, 2007); X_u^+, Z_u^+ and M_u^+, non-dimensional derivatives of the x- and z-component of the aerodynamic force and aerodynamic moment, respectively, with respect to the x-component (u^+) of the non-dimensional velocity; X_w^+, Z_w^+ and M_w^+, non-dimensional derivatives of the x- and z-component of the aerodynamic force and aerodynamic moment, respectively, with respect to the z-component (w^+) of the non-dimensional velocity; X_q^+, Z_q^+ and M_q^+, non-dimensional derivatives of the x- and z-component of the aerodynamic force and aerodynamic moment, respectively, with respect to the non-dimensional pitching rate (q^+).

Table 8. Non-dimensional stability derivatives normalized by non-dimensional mass or moment of inertia

ID	X_u^+/m^+	Z_u^+/m^+	$M_u^+/I_{y,b}^+$	X_w^+/m^+	Z_w^+/m^+	$M_w^+/I_{y,b}^+$	X_q^+/m^+	Z_q^+/m^+	$M_q^+/I_{y,b}^+$	g^+
HF1	−0.027	0.003	0.110	0.003	−0.029	0.026	−0.004	−0.002	−0.008	−0.029
HF1$_{rot}$	−0.021	−0.006	0.111	0.001	−0.028	−0.032	−0.005	−0.001	−0.008	−0.029
HF$_{norm}$	−0.020	−0.001	0.199	0.000	−0.020	0.004	−0.004	0.000	−0.003	−0.023

HF1, hoverfly 1; HF1$_{rot}$, hoverfly 1 rotated to normal hovering; HF$_{norm}$, hoverfly studied by Sun and Wang in normal hovering (Sun and Wang, 2007); definitions of X_u^+, Z_u^+ etc., as in Table 7; m^+, non-dimensional mass; $I_{y,b}^+$, non-dimensional moment of inertia; g^+, non-dimensional gravitational acceleration.

where g is the gravitational acceleration; X_u, Z_u, etc. are the aerodynamic derivatives [for example, X_u is the derivative of X with respect to u (X and Z are the x- and z-components of the aerodynamic force, respectively)]; M is the aerodynamic pitching moment (x and z are coordinate axes fixed on the body with the origin at the center of mass; at equilibrium flight, i.e. hovering, x is horizontal, pointing forward, and z is vertical, pointing downward); u and w are the x- and z-components of the velocity of the center of mass; and q is the pitching rate of the body. For comparison with other insects, non-dimensional quantities are used: X_u, X_w, etc. are non-dimensionalized by $0.5\rho U(2S)$; X_q and Z_q by $0.5\rho U^2(2S)/f$; M_u and M_w by $0.5\rho U(2S)c$; M_q by $0.5\rho U^2(2S)c/f$; m by $0.5\rho U(2S)/f$; $I_{y,b}$ by $0.5\rho U^2(2S)/f^2$; and g by Uf [we use the superscript '+' to denote a non-dimensional quantity, e.g. $X_u^+ = X_u/0.5\rho U^2(2S)$].

The computed aerodynamic derivatives of HF1 are given in Table 7. Sun and Wang conducted longitudinal stability analysis of a hoverfly in normal hovering (Sun and Wang, 2007); here, we call this hoverfly HF$_{norm}$. For comparison, the aerodynamic derivatives of HF$_{norm}$ are included in Table 7. We also computed the stability derivatives with HF1 rotated to normal hovering (in the same way as done in the power analysis); the insect in this case is denoted as HF1$_{rot}$. The aerodynamic derivatives of HF1$_{rot}$ are also given in Table 7.

As seen in Eqn 2, the elements of the system matrix, and hence the stability properties, are determined not only by the aerodynamic derivatives, but also by the derivatives divided by the mass or moment of inertia of the insect. The derivatives, normalized by mass or moment of inertia, i.e. X_u^+/m^+, Z_u^+/m^+, etc., are shown in Table 8. The difference in each element of the system matrix between HF1 and HF1$_{rot}$ is very small; there is some difference between HF1 and HF$_{norm}$, but it is not very large. This indicates that the eigenvalues and eigenvectors, and hence the stability properties of HF1, HF1$_{rot}$ and HF$_{norm}$, would not be very different.

The eigenvalues for the three cases are shown in Table 9. As anticipated, there is little difference in the eigenvalues between HF1 and HF1$_{rot}$, and only a small difference between HF1 and HF$_{norm}$ (this is also true for the eigenvectors; data not shown).

The system matrix or the eigenvalues and eigenvectors represent the inherent property of a flight system: the less stable

a system is, the easier it is to change its state. The above results, especially the results of HF1 and HF1$_{rot}$ (the same insect in inclined stroke-plane hovering and in normal hovering), show that stability properties are almost the same for the two types of hovering. Thus, we see that the two types of hovering have little difference in maneuverability.

APPENDIX
Measurement method and error assessment
Measuring wing and body kinematics

The method of measuring the kinematic parameters of the body and wings using the filmed data is based on stereovision-based triangulation (see Fry et al., 2003; Fry et al., 2005; Liu and Sun, 2008; Belhaoua et al., 2009; Ristroph et al., 2009; Walker et al., 2009). The general structure of a trinocular stereo vision system is shown in Fig. A1 [in the figure, (X_w, Y_w, Z_w) is the world coordinate system; (X_{C1}, Y_{C1}, Z_{C1}), (X_{C2}, Y_{C2}, Z_{C2}) and (X_{C3}, Y_{C3}, Z_{C3}) are the camera coordinate systems of camera 1, 2 and 3, respectively; and (u_1, v_1), (u_2, v_2) and (u_3, v_3) are the image coordinate systems of camera 1, 2 and 3, respectively]. Based on the basic principles of stereo vision, the projections of the scene point in the world coordinate system onto any image coordinate system can be calculated on the condition that the point's coordinate in the world coordinate system and projection matrices are known. The calculation procedure is as follows.

Let P be an arbitrary point, whose coordinates are X_w, Y_w and Z_w in the world frame and X_{C1}, Y_{C1} and Z_{C1} in the frame of camera 1. Let p_1 be the projective point of P on camera 1; p_1's coordinates in the image frame of camera 1 are u_1 and v_1. The coordinate

Table 9. Non-dimensional eigenvalues of the system matrix

ID	$\lambda_{1,2}$	λ_3	λ_4
HF1	0.062±0.128i	−0.158	−0.030
HF1$_{rot}$	0.064±0.129i	−0.156	−0.030
HF$_{norm}$	0.074±0.144i	−0.171	−0.020

HF1, hoverfly 1; HF1$_{rot}$, hoverfly 1 rotated to normal hovering; HF$_{norm}$, hoverfly studied by Sun and Wang in normal hovering (Sun and Wang, 2007). $\lambda_{1,2}$, a pair of complex conjugate eigenvalues; λ_3 and λ_4, real eigenvalues.
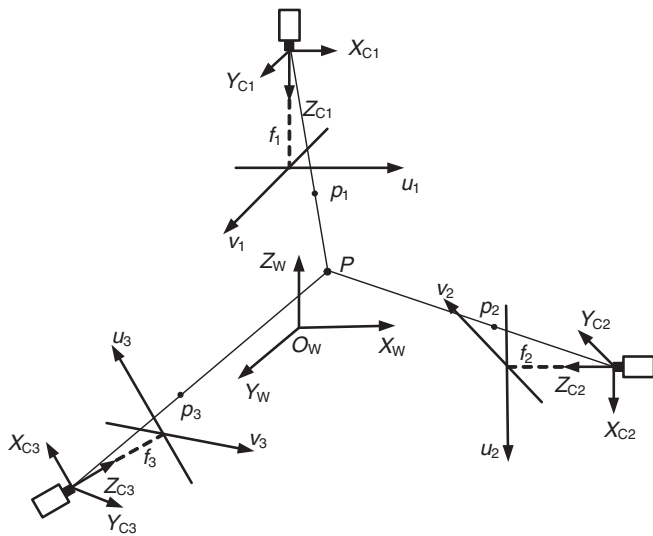
Fig. A1. Model of trinocular stereo vision system. (X_w Y_w Z_w), world coordinate system; (X_{C1} Y_{C1} Z_{C1}), (X_{C2} Y_{C2} Z_{C2}) and (X_{C3} Y_{C3} Z_{C3}), camera coordinate systems of cameras 1, 2 and 3, respectively; (u_1, v_1), (u_2, v_2) and (u_3, v_3), image coordinate systems of cameras 1, 2 and 3, respectively. f_1, f_2 and f_3, the focal length of cameras 1, 2 and 3, respectively; P, an arbitrary point; p_1, p_2 and p_3, the projective points of P on cameras 1, 2 and 3, respectively.

transformation between the world coordinate system and the image coordinate systems is:

$$Z_{C1} \begin{bmatrix} u_1 \\ v_1 \\ 1 \end{bmatrix} = \boldsymbol{M}_1 \begin{bmatrix} X_w \\ Y_w \\ Z_w \\ 1 \end{bmatrix}, \qquad (A1)$$

where $\boldsymbol{M}_1$ is the projection matrix of camera 1 (the projection matrix is determined by camera calibration, see below). Let $m1_{i,j}$ (i, j=1, 2, 3) denote the elements of $\boldsymbol{M}_1$. Eliminating Z_{C1} from Eqn A1 gives:

$$\begin{cases} m1_{11} X_w + m1_{12} Y_w + m1_{13} Z_w + m1_{14} - u_1 X_w m1_{31} \\ \quad - u_1 Y_w m1_{32} - u_1 Z_w m1_{33} = u_1 \\ m1_{21} X_w + m1_{22} Y_w + m1_{23} Z_w + m1_{24} - v_1 X_w m1_{31} \\ \quad - v_1 Y_w m1_{32} - v_1 Z_w m1_{33} = v_1 \end{cases} . \quad (A2)$$

The coordinates of point P's projection onto the image coordinate system of camera 1 can be determined *via* Eqn A2. By consecutively replacing $\boldsymbol{M}_1$ by projection matrices of camera 2 ($\boldsymbol{M}_2$) and camera 3 ($\boldsymbol{M}_3$) and repeating the above calculation, we can obtain all projections on the three image coordinate systems.

We use a line segment, whose length is equal to the body length of the insect, to represent the body of the insect, and the outline of the wing, obtained from scanning the wing (see Fig. 1A), to represent the wing. The line segment of the body and the outline of a wing are referred to as the models of the body and the wing, respectively. Each of them is represented as a set of points. Using the method described above, we could easily compute the projection of the point set on all the three image coordinate systems.

We put the models of the body and the wings into the world coordinate system, then change the positions and orientations of those models until the best overlap between a models' projection and the displayed frame is achieved in all three views. At this point,

the positions and orientations of those models would be taken as the positions and orientations of the body and wings of the insect. Generally, several re-adjustments of each model's position and orientation are required to obtain a satisfactory overlap. The matching is done manually. We have developed a graphical user interface subroutine for MATLAB to execute the above procedures.

Camera calibration

We used a flat glass panel with a high accuracy black-and-white checkerboard pattern printed on it to calibrate the three orthogonally aligned cameras. The calibration gave the intrinsic and extrinsic parameters of each camera (these parameters determined the transform matrix of the camera). Each image of the calibration panel contained 324 automatically identified corner points as required feature points. Fifty-five of the 90 images of the calibration panel were used for calibrating each single camera and the stereo rigs. The calibrations were carried out using a custom-written program in MATLAB.

Error analysis

The stereovision-based triangulation method has several types of error (Belhaoua et al., 2009). In the present case, the errors are due to camera model inaccuracy (pinhole model was used to characterize the cameras), camera calibration, stereo rig calibration and discretization (the projection of a 3-D point in the image plane is approximated to the nearest pixel). Another error source is wing deformation. Insect wings have time-dependent deformation during flapping motion. Our model of the wing is a rigid flat plate that has the same outline as the cut-off wing, and errors will arise when one tries to match the model's projection with the image of the flapping wing.

Errors due to the camera model, camera calibration and stereo rig calibration are categorized as system error. Thirty-five images of the calibration panel that had not been used in calibrating the cameras were used to estimate these errors and the results were as follows. We used the reprojected pixel error (RPE) (Walker et al., 2009) as an indicator of camera model accuracy. For all three cameras, the RPE was less than 0.16 pixels in both directions on the image plane. Adding distortion and/or skew parameters to the pinhole model did not reduce the RPE significantly. Accuracy in describing the relative orientation and position between every two cameras was 0.02 deg and 0.03 mm, respectively. In the above processes, all computations reached a sub-pixel level accuracy based on the features detected, so the results were not affected by the discretization errors, which will be considered below.

The above results show that errors due to the camera model, camera calibration and stereo rig calibration are very small. It is expected that the other two types of errors, i.e. discretization errors and errors due to wing deformation, are the primary errors of the method. Here, we estimate these two types of errors as a whole; this estimate will be taken as the error of the method.

To estimate discretization and wing deformation errors, we applied our method to a computer-generated virtual insect consisting

Fig. A2. An example of the of the virtual insect (A) and its three projective images (B,C,D).
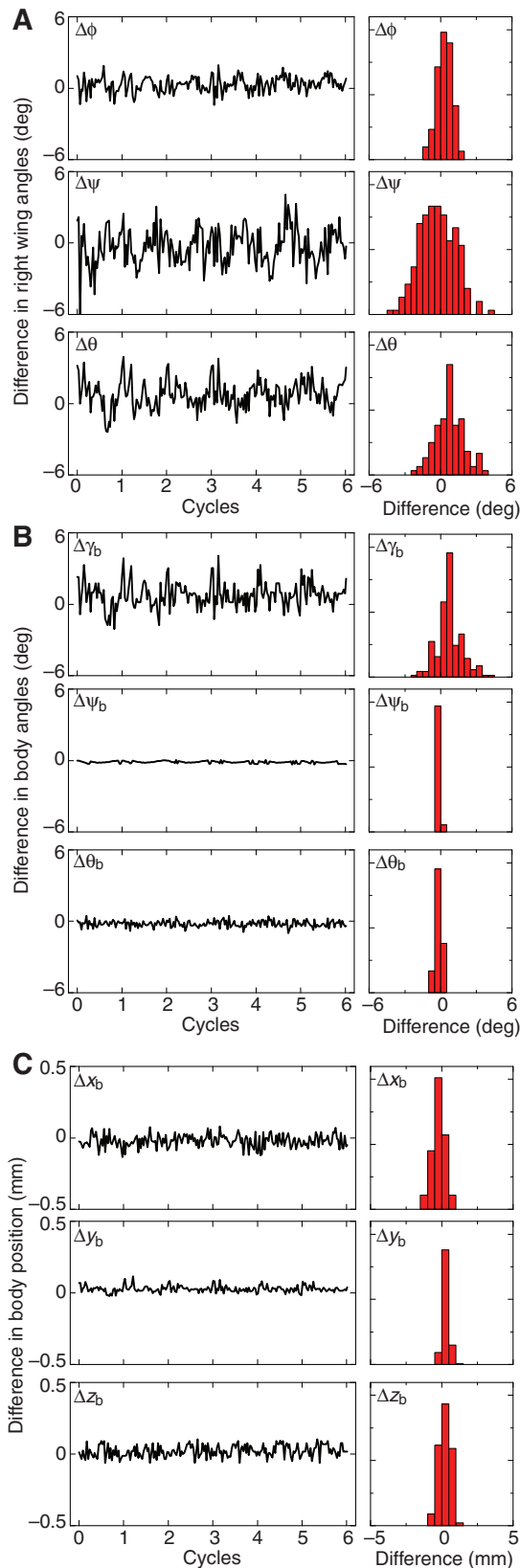
Fig. A3. Differences between the measured and imposed wing and body kinematic parameters (measured value minus imposed value; 'Δ' denotes difference). (A) Right wing angles: ϕ, positional angle; θ, elevation angle; ψ pitch angle. (B) Body angles: ψ_b, yaw angle; θ_b, pitch angle; γ_b, roll angle. (C) Position of body center of mass: x_b, y_b and z_b, horizontal, sidewise and vertical displacements of the body center of mass, respectively.

of a rigid body and two deforming wings. The wings can rotate around their roots (being joints with three degrees of freedom) and have time-dependent twist and camber deformations. The body is unrestrained in space, having six degrees of freedom. The wing and body motions and the wing deformation of the virtual insect are as follows. The positional and elevation angles and the pitch angle at r_2 of the wing are set the same as those of HF1. Based on observations of flight in many insects (Walker et al., 2009; Ellington, 1984b; Ennos, 1989a), the wing is assumed to have a 15 deg twist and 6% camber during the translation phase of the downstroke or upstroke and the twist and camber increase to 25 deg and 10%, respectively, at stroke reversal. It is assumed that the center of mass of the body has a horizontal harmonic oscillation of 2.5 mm amplitude and the pitch angle of the body has a harmonic oscillation of 5 deg amplitude. Each wingbeat cycle contains 35 data points.

First, we used the projection matrices to project the virtual insect onto the image planes of the cameras (setting the resolution and pixel ratio the same as those of the real cameras) and obtained three nearly orthogonal projective images of the virtual insect (an example of the 3-D virtual insect and its images is given in Fig. A2). This step contains the discretization errors. Next, as was done in the real experiment, we represented the virtual insect by the body and wing models (body represented by a line segment and wing represented by its outline; each of the models was a set of points). We put the models of the body and the wings into the world coordinate system and then changed the positions and orientations of the models until the best overlap between each model's projection and the corresponding image of the virtual insect was achieved in all three views. We thus obtained the measurements of body and wing kinematics of the virtual insect.

Comparison between the measured and the imposed body and wing kinematics gives the errors. Six wingbeats were analyzed. Fig. A3 shows the differences between the measured and imposed kinematic parameters and the corresponding histograms for the body and the right wing (results for the left wing are similar). As seen in Fig. A3A, for positional angle and elevation angle of the wing, errors are within 3 deg and the residuals are nearly centered around zero, indicating that there are only small systematic deviations; for the pitch angle of the wing, errors are a little larger, within 4 deg. For the body orientation (Fig. A3B), errors in yaw and pitch angles are approximately 1 deg and error in roll angle is within 3 deg. Errors in the body position (Fig. A3C) are typically less than 0.2 mm, or 2% of body length.

LIST OF SYMBOLS

A	system matrix
c	mean chord length
C_D	wing drag coefficient
C_G	weight coefficient
C_H	horizontal force coefficient
C_L	wing lift coefficient
C_p	non-dimensional power
C_V	vertical force coefficient
$\overline{C}_V$	mean vertical force coefficient
D	drag of a wing
f	stroke frequency
$\boldsymbol{g}$	gravitational acceleration
H	horizontal force
h_1	distance from wing-root axis to long axis of the body
$I_{x,b}, I_{y,b}, I_{z,b}$	moments of inertia of the body about the center of mass of the body
$I_{x,w}, I_{y,w}, I_{z,w}$	moments of inertia of a wing about the wing root
$I_{xz,b}$	product of inertia of the body
$I_{xz,w}$	product of inertia of a wing

J	advance ratio
L	lift of a wing
l_1	distance from wing-root axis to body center of mass
l_2	distance from anterior end of body to center of mass
l_b	body length
l_r	distance between two wing roots
m	mass of an insect
M	total aerodynamic pitching moment about center of mass
M_a	aerodynamic moment of wing around wing root
M_i	inertial moment of wing around wing root
M_q	derivative of M with respect to q
M_u	derivative of M with respect to u
M_w	derivative of M with respect to w
m_{wg}	mass of one wing
P^*	body-mass-specific power
P_a	aerodynamic power
P_i	inertial power
q	pitching angular velocity about the center of mass
R	wing length
r_2	radius of the second moment of wing area
S	area of one wing
t	time
t_c	wingbeat period
$\hat{t}$	non-dimensional time ($\hat{t}=0$ and 1 at the start and end of a cycle, respectively)
u	component of velocity along the x-axis
U	reference velocity (mean flapping velocity at r_2)
V	vertical force of a wing
w	component of velocity along the z-axis
X	x-component of the total aerodynamic force
x, y, z	coordinates in the body-fixed frame of reference (with origin at center of mass)
X_q	derivative of X with respect to q
X_u	derivative of X with respect to u
X_w	derivative of X with respect to w
Z	z-component of the total aerodynamic force
Z_q	derivative of Z with respect to q
Z_u	derivative of Z with respect to u
Z_w	derivative of Z with respect to w
$^+$	non-dimensional quantity
α	angle of attack of wing
β	stroke plane angle
θ	deviation angle of wing
λ	generic notation for an eigenvalue
ρ	density of fluid
ϕ	positional angle of wing
$\bar{\phi}$	mean positional angle
Φ	stroke amplitude
χ	body angle
ψ	pitch angle of wing
Ω	wing rotation velocity vector

ACKNOWLEDGEMENTS

REFERENCES

Aono, H., Liang, F. and Liu, H. (2008). Near- and far-field aerodynamics in insect hovering flight: and integrated computational study. *J. Exp. Biol.* **211**, 239-257.

Belhaoua, A., Kohler, S. and Hirsch, E. (2009). Estimation of 3D reconstruction errors in a stereo-vision system. In *Modeling Aspects in Optical Metrology II*, Vol. 7390 (ed. H. Bosse, B. Bodermann and R. M. Silver), pp. 73900X-73900X-10. Munich, Germany: SPIE.

Bergou, A. J., Ristroph, L., Guckenheimer, J., Cohen, I. and Wang, Z. J. (2010). Fruit flies modulate passive wing pitching to generate in-flight turns. *Phys. Rev. Lett.* **104**, 148101.

De Geer, C. (1776). *Memoires pour Servir a l'Histoire des Insects*. Stockholm: L. L. Grefing.

Dickinson, M. H., Lehmann, F. O. and Sane, S. P. (1999). Wing rotation and the aerodynamic basis of insect flight. *Nature* **284**, 1954-1960.

Dickson, W. B., Straw, A. D. and Dickinson, M. H. (2008). Integrative model of *Drosophila* flight. *AIAA J.* **46**, 2150-2164.

Du, G. and Sun, M. (2010). Effects of wing deformation on aerodynamic forces in hovering hoverflies. *J. Exp. Biol.* **213**, 2273-2283.

Ellington, C. P. (1984a). The aerodynamics of hovering insect flight. II. Morphological parameters. *Philos. Trans. R. Soc. Lond. B* **305**, 1-15.

Ellington, C. P. (1984b). The aerodynamics of hovering insect flight. III. Kinematics. *Philos. Trans. R. Soc. Lond. B* **305**, 17-40.

Ellington, C. P., Van Den Berg, C., Willmott, A. P. and Thomas, A. L. R. (1996). Leading-edge vortices in insect flight. *Nature* **384**, 626-630.

Ennos, A. R. (1989a). The kinematics and aerodynamics of the free flight of some Diptera. *J. Exp. Biol.* **142**, 49-85.

Ennos, A. R. (1989b). Inertial and aerodynamic torques on the wings of Diptera in flight. *J. Exp. Biol.* **142**, 87-95.

Fry, S. N., Sayaman, R. and Dickinson, M. H. (2003). The aerodynamics of free-flight maneuvers in *Drosophila*. *Science* **300**, 495-498.

Fry, S. N., Sayaman, R. and Dickinson, M. H. (2005). The aerodynamics of hovering flight in *Drosophila*. *J. Exp. Biol.* **208**, 2303-2318.

Hilgenstock, A. (1988). A fast method for the elliptic generation of three dimensional grids with full boundary control. In *Numerical Grid Generation in CFM'88* (ed. S. Sengupta, J. Hauser, P. R. Eiseman and J. F. Thompson), pp. 137-146. Swansea, UK: Pineridge Press Ltd.

Liu, H., Ellington, C. P., Kawachi, K., Van Den Berg, C. and Willmott, A. P. (1998). A computational fluid dynamic study of hawkmoth hovering. *J. Exp. Biol.* **201**, 461-477.

Liu, Y. and Sun, M. (2008). Wing kinematics measurement and aerodynamics of hovering droneflies. *J. Exp. Biol.* **211**, 2014-2025.

Luo, G. L. and Sun, M. (2005). The effects of corrugation and wing planform on the aerodynamic force production of sweeping model insect wings. *Acta Mech. Sinica* **21**, 531-541.

Norberg, R. A. (1975). Hovering flight of the dragonfly *Aeschna juncea* L., kinematics and aerodynamics. In *Swimming and Flying in Nature* (ed. T. Y. Wu, C. J. Brokaw and C. Brennen), pp. 763-781. New York: Plenum Press.

Ristroph, L., Berman, G. J., Bergou, A. J., Wang, Z. J. and Cohen, I. (2009). Automated hull reconstruction motion tracking (HRMT) applied to sideways maneuvers of free-flying insects. *J. Exp. Biol.* **212**, 1324-1335.

Rogers, S. E. and Kwak, D. (1990). Upwind differencing scheme for the time-accurate incompressible Navier-Stokes equations. *AIAA J.* **28**, 253-262.

Rogers, S. E., Kwak, D. and Kiris, C. (1991). Steady and unsteady solutions of the incompressible Navier-Stokes equations. *AIAA J.* **29**, 603-610.

Sane, S. P. and Dickinson, M. H. (2001). The control of flight force a flapping wing: lift and drag production. *J. Exp. Biol.* **204**, 2607-2626.

Sun, M. and Du, G. (2003). Lift and power requirements of hovering insect flight. *Acta Mech. Sinica* **19**, 458-469.

Sun, M. and Tang, J. (2002a). Unsteady aerodynamic force generation by a model fruit fly wing in flapping motion. *J. Exp. Biol.* **205**, 55-70.

Sun, M. and Tang, J. (2002b). Lift and power requirements of hovering flight in *Drosophila virilis*. *J. Exp. Biol.* **205**, 2413-2427.

Sun, M. and Wang, J. K. (2007). Flight stabilization control of a hovering model insect. *J. Exp. Biol.* **210**, 2714-2722.

Sun, M. and Xiong, Y. (2005). Dynamic flight stability of a hovering bumblebee. *J. Exp. Biol.* **208**, 447-459.

Taylor, G. K. and Thomas, A. L. R. (2003). Dynamic flight stability in the desert locust *Schistocerca gregaria*. *J. Exp. Biol.* **206**, 2803-2829.

Usherwood, J. R. and Ellington, C. P. (2002). The aerodynamics of revolving wings. II. Propeller force coefficients from mayfly to quail. *J. Exp. Biol.* **205**, 1565-1576.

Wakeling, J. M. and Ellington, C. P. (1997). Dragonfly flight. II. Velocities, accelerations and kinematics of flapping flight. *J. Exp. Biol.* **200**, 557-582.

Walker, S. M., Thomas, A. L. R. and Taylor, G. K. (2009). Photogrammetric reconstruction of high-resolution surface topographies and deformable wing kinematics of tethered locusts and free-flying hoverflies. *J. R. Soc. Interface* **6**, 351-366.

Walker, S. M., Thomas, A. L. R. and Taylor, G. K. (2010). Deformable wing kinematics in free-flying hoverflies. *J. R. Soc. Interface* **7**, 131-142.

Wang, Z. J. (2000). Two dimensional mechanism for insect hovering. *Phys. Rev. Lett.* **85**, 2216-2219.

Wang, Z. J. and Russell, D. (2007). Effect of forewing and hindwing interactions on aerodynamic forces and power in hovering dragonfly flight. *Phys. Rev. Lett.* **99**, 148101.

Wang, Z. J., Birch, J. M. and Dickinson, M. H. (2004). Unsteady forces and flows in low Reynolds number hovering flight: two-dimensional computations vs robotic wing experiments. *J. Exp. Biol.* **207**, 449-460.

Weis-Fogh, T. (1973). Quick estimates of flight fitness in hovering animals, including novel mechanism for lift production. *J. Exp. Biol.* **59**, 169-230.

Wu, J. H., Zhang, Y. L. and Sun, M. (2009). Hovering of model insects: simulation by coupling equations of motion with Navier-Stokes equations. *J. Exp. Biol.* **212**, 3313-3329.

Yu, X. and Sun, M. (2009). A computational study of the wing-wing and wing-body interactions of a model insect. *Acta Mech. Sinica* **25**, 421-431.